

# A Multiple-Regime Approach to Atmospheric Zonal-Flow Vacillation

by

Seongjoon Koo

Andrew W. Robertson

and

Michael Ghil

Department of Atmospheric Sciences and  
Institute of Geophysics and Planetary Physics  
University of California, Los Angeles  
Los Angeles, CA 90095-1565

June 24, 2000

*J. Atmos. Sci.*, revised

Corresponding author's address:

Seongjoon Koo

Department of Atmospheric Sciences

University of California, Los Angeles

Los Angeles, CA 90095-1565

E-mail: [koo@atmos.ucla.edu](mailto:koo@atmos.ucla.edu)

Phone: (310) 825-7407

Fax: (310) 206-5219

# Abstract

Zonal-flow vacillation in an idealized two-layer, global, primitive-equation model is studied in the context of multiple regimes. The spatial structure of vertically and zonally averaged zonal-flow variability resembles that observed in the Southern Hemisphere, with dipolar anomalies centered at  $40^\circ$  and  $60^\circ$ .

The probability density function (PDF) of the model's zonal flow is studied in the subspace of its two leading principal components. The PDF exhibits multiple regimes consisting of a pronounced central peak with two distinct shoulders attached to it. All three features are statistically significant at the 95% confidence level against the null hypothesis of a two-dimensional Markov process of order one. Flow composites for the two shoulders show meteorologically significant differences from climatology and similarities with observed Southern Hemisphere flow patterns. In the low-latitude regime the narrow jet's maximum lies equatorward of the climatological mean position, while in the high-latitude regime the broad jet is sometimes bimodal and has its maximum poleward of the climatological position. The residence times in the high- and low-latitude regimes are typically 2–3 times as long as in the central-peak regime.

Both regimes' onsets are found to be abrupt, but the regime breaks exhibit a significant asymmetry: the low-latitude regime decays more slowly, while the high-latitude regime breaks rather abruptly. Eddy momentum forcing acts to maintain the zonal-flow regimes against surface drag. The changes in low-level eddy heat flux precede those of the eddy momentum forcing that drive both the regime onset and break. This phase difference between heat and momentum fluxes suggest that baroclinic processes play an important role in the regime transitions. The dependence of the preferred regimes' zonal-jet latitudes on bottom friction shows that multiple regimes coexist in a wide range of the parameter values.

# 1 Introduction

The zonally averaged zonal flow in the Southern Hemisphere (SH) exhibits pronounced low-frequency variability (LFV) on intraseasonal (Webster and Keller 1975) and interannual (Trenberth 1979) time scales. The dominant mode of the observed variability (Kidson 1988; Hartmann and Lo 1998) exhibits an equivalent barotropic vertical structure with dipolar anomalies centered near 40°S and 60°S. Recent observations (Hartmann and Lo 1998) indicate that there are no significant spectral peaks associated with this mode, although the mean duration of the extreme phases is estimated as 6.2 to 8.6 days. We shall use the term *zonal-flow vacillation* to indicate the irregular and aperiodic variations of the SH zonal jet.

Zonal-flow vacillation between two persistent anomalous states with irregular transitions between them suggests the concept of multiple regimes that originated in the work of Charney and DeVore (1979). The extent to which the LFV of planetary-scale atmospheric motion is well described by a small set of multiple regimes with abrupt transitions among them has been hotly debated. There is growing evidence, however, that observed atmospheric LFV in both the Northern Hemisphere (NH) and SH can be well described in these terms (Hansen and Sutera 1986; Mo and Ghil 1987, 1988; Mechoso et al. 1991; Cheng and Wallace 1993; Kimoto and Ghil 1993a, b; Michelangeli et al. 1995; Smyth et al. 1999).

Several attempts have been made to identify multiple regimes and bimodality associated with SH zonal-flow vacillation. Based on visual inspection of the zonal jet's position, Yoden et al. (1987) found two distinct flow regimes during the 1980–1983 austral winters, corresponding to single- and double-jet states. Akahori and Yoden (1997) studied the relationship between zonal-flow vacillation and wave breaking patterns of baroclinic eddies using an idealized model. They found bimodality in a histogram plot of an empirical measure of the typical latitude of wave breaking associated with the zonal-flow vacillation, the so-called LC index. However, no bimodality was found in a histogram of the zonal-mean flow's first

principal component (PC-1). Hartmann and Lo (1998) also reported finding no bimodality in PC-1 of the zonal-mean SH flow.

The main characteristics of zonal-flow vacillation and the dynamics of its two extreme phases are now relatively well understood. Modeling studies by Robinson (1991) and Yu and Hartmann (1993) and an observational study by Hartmann and Lo (1998) strongly suggest that both of the vacillation's extreme phases are maintained by the organized feedback between the zonal flow and the transient eddies.

High-frequency, synoptic-scale eddies with a period of less than 10 days play a key role in this feedback (Robinson 1991; Yu and Hartmann 1993). An observational study by Feldstein and Lee (1998) also found evidence of the feedback between the zonal flow and high-frequency eddies, although the feedback was less clear when the eddies were not filtered (Lee and Feldstein 1996; Feldstein and Lee 1996). Using an idealized model, Robinson (1996) demonstrated that the feedback depends upon the strength of bottom friction, and is prominent only for sufficiently strong surface friction. Robinson (2000) proposed a simple baroclinic mechanism based on quasi-geostrophic dynamics to explain this feedback.

Despite the advances in our understanding of the extreme phases described above, the dynamics of the *transient* phases of the vacillation remains poorly understood. For example, the origin of the initial eddy forcing that drives the zonal flow into one of the extreme phases is not clear. Nor is it known what causes these two relatively persistent phases of the vacillation to break.

In the present study we examine the probability density function (PDF) of the zonal flow in the simplified setting of an idealized atmospheric model of the type used by Hendon and Hartmann (1985). Our aim is to clarify the issue of multiple regimes, and to improve our understanding of the underlying dynamics. In our study, unlike previous studies, the vacillation's two extreme phases are explicitly shown to constitute two recurrent flow regimes. The time evolution of the vacillation is then more easily traced in phase space as well

as in physical space, and composites with respect to onset and break of the two extreme phases of the vacillation can be constructed in a natural fashion. Previous observational studies (Kidson 1988; Hartmann and Lo 1998) suggest that the vacillating zonal jet in the SH is mainly an eddy-driven mid-latitude phenomenon. This allows us to capture the fundamental dynamics of the zonal-flow vacillation using a relatively simple model, with no asymmetries in its lower boundary. Our simple model can easily be integrated for the long time spans required to obtain reliable statistics of the regimes and their entire evolution, from onset to break.

This paper is organized as follows: the numerical model is described in Section 2 and the multiple regimes of its zonal-mean flow are discussed in Section 3. In Section 4, we examine the time evolution of the vacillating zonal jet, with emphasis on the onset and break of the vacillation’s two extreme phases. The role of surface friction is investigated in Section 5 using additional sensitivity runs. A summary and discussion of the main results are provided in Section 6.

## 2 Model

The model used in this study is based on the atmospheric component of Saravanan and McWilliams’ coupled model (1995) and is very similar to the two-layer model of Hendon and Hartmann (1985). It is a dry primitive-equation model on a sphere. The governing equations in pressure coordinates are

$$\frac{\partial \zeta}{\partial t} = -\nabla \cdot (\zeta + f)\mathbf{V} - \mathbf{k} \cdot \nabla \times \left( \omega \frac{\partial \mathbf{V}}{\partial p} - \mathbf{F} \right), \quad (1)$$

$$\frac{\partial D}{\partial t} = \mathbf{k} \cdot \nabla \times (\zeta + f)\mathbf{V} - \nabla \cdot \left( \omega \frac{\partial \mathbf{V}}{\partial p} - \mathbf{F} \right) - \nabla^2 \left( \frac{\mathbf{V} \cdot \mathbf{V}}{2} + \Phi \right), \quad (2)$$

$$\frac{\partial \theta}{\partial t} = -\nabla \cdot (\theta \mathbf{V}) - \frac{\partial}{\partial p}(\theta \omega) + Q, \quad (3)$$

$$\nabla \cdot \mathbf{V} + \frac{\partial \omega}{\partial p} = 0, \quad (4)$$

$$\frac{\partial \Phi}{\partial p} = -\frac{R\theta}{p} \left( \frac{p}{p_0} \right)^{\frac{R}{c_p}}; \quad (5)$$

here  $\mathbf{k}$  denotes the vertical unit vector,  $\nabla$  the horizontal gradient operator,  $\mathbf{V} \equiv (u, v)$  the horizontal velocity,  $\zeta = \mathbf{k} \cdot \nabla \times \mathbf{V}$  the vertical component of relative vorticity,  $D = \nabla \cdot \mathbf{V}$  the horizontal divergence,  $\Phi \equiv gz$  the geopotential,  $\omega$  the vertical velocity in pressure coordinates,  $\theta$  the potential temperature,  $p_0$  the surface pressure at 1000 hPa,  $\mathbf{F}$  the mechanical forcing, and  $Q$  the thermal forcing.

The above equations are discretized in the vertical following Lorenz (1960): the two layers have the same thickness,  $\Delta p = 500$  hPa, and are centered at 250 hPa and 750 hPa. Due to the homogeneous lower boundary, boundary conditions are simply  $\omega = 0$  at  $p = 0$  and 1000 hPa. Even though the two-level configuration is a crude representation of the atmosphere, it has been used extensively and its properties are well documented. Hendon and Hartmann (1985) and Keppenne et al. (2000), in particular, reported that a two-level global primitive-equation model can produce realistic low-frequency behavior. Simple two-layer models have also been proven useful in theoretical studies of zonal-flow vacillation (Robinson 1991, 1996; Lee and Feldstein 1996) and in the study of advanced data assimilation methods (Ghil and Todling 1996).

For horizontal discretization, we adopt triangular truncation at T21. This relatively low resolution has been shown to capture the essential features of zonal-flow vacillation (Yu and Hartmann 1993) and is in accordance with the simple 2-level discretization in the vertical. Comparable horizontal resolutions have been adopted in other previous studies of

the problem at hand (Robinson 1991, 1996; Lee and Feldstein 1996). The time step is equal to 1 hour and results are saved every 24 hours.

The mechanical and thermal forcing terms within each model layer are chosen as follows:

$$\mathbf{F}_i = \gamma(\nabla^2 + \frac{2}{a^2})^4 \mathbf{V}_i - \frac{\delta_{i,2}}{\tau_E} \mathbf{V}_i, \quad (6)$$

$$Q_i = \gamma(\nabla^2)^4 \theta_i - \eta(\theta_i - \theta_{e,i}); \quad (7)$$

$i = 1, 2$  denote the upper and lower model levels, at 250 hPa and 750 hPa, respectively and  $\delta_{i,j}$  represents the Kronecker delta. The scale-selective damping coefficient  $\gamma$  is chosen to act with a time scale of 1/4 day on the highest wavenumber resolved at our T21 truncation (Saravanan and McWilliams 1995). The Earth's radius is  $a = 6.4 \times 10^6$  m and the Ekman drag time scale  $\tau_E$  is set to be 3 days. The radiative relaxation coefficient  $\eta$  is  $15^{-1}$  days $^{-1}$ . The radiative equilibrium potential temperature  $\theta_e$  is prescribed to simulate perpetual-winter conditions, as in Hendon and Hartmann (1985).

The model with the parameter values described above was run for 30000 days and the first 300 days are discarded to avoid any initial transients. This model run is described and analyzed in Sections 3 and 4, while additional runs are studied in Section 5.

### 3 Multiple regimes in zonal-mean flow

#### *a. PDF estimation*

We apply a nonparametric density-estimation technique to search for multiple regimes in the latitudinal position of the model's jet. A multivariate kernel density estimator (Silverman 1986) is used to estimate the PDF of the zonally and vertically averaged zonal-wind profile from the time series of 29700 daily profiles. This method was previously used by Kimoto and Ghil (1993a, b) to identify multiple flow regimes in the NH observed winter-time circulation.

First, a 10-day low-pass filter is applied to the time series of the zonally and vertically averaged zonal wind. The 31-point nonrecursive digital filter employs Lanczos smoothing to avoid Gibbs phenomena. Empirical orthogonal function (EOF) analysis was then performed on the low-pass filtered data by diagonalizing the covariance matrix. The filtering has little effect on the resulting EOF structures, although the fraction of variance described by the leading EOF increases slightly.

Figure 1 shows the two leading EOFs, which account for 62.1% and 17.2% of total variance, respectively. EOF-1 exhibits dipolar variability with maxima of opposite signs centered near 40° and 60°. Its node is located at 48°, which corresponds to the position of the model’s climatological zonal jet maximum. Thus, EOF-1 represents the zonal jet’s meridional displacement from its climatological mean position. The spatial structure of EOF-1 resembles its observed SH counterpart quite closely (Kidson 1988; Hartmann and Lo 1998), in spite of our model’s high degree of idealization. The second EOF exhibits an extremum near 50°, and is thus primarily associated with a strengthening and weakening of the climatological zonal jet.

[ Figure 1 near here, please ]

Temporal variability of the model-simulated flows is investigated by projecting the *unfiltered* zonally and vertically averaged zonal wind anomalies onto the low-pass filtered EOFs. This produces time series whose length equals that of the original dataset of 29700 daily profiles.

Before discussing details of PDF estimation, we first consider data scatter in phase space and its implications for PDF estimation. Data scatter in terms of “signal” and “noise” is illustrated in Fig. 2 following Kimoto and Ghil (1993a). In Figs. 2a and 2b, the abscissa denotes the signal component defined by

$$||\mathbf{x}||_s \equiv \left( \sum_{i=1}^s c_i^2 \right)^{1/2}, \quad (8)$$



and the ordinate indicates the noise component defined by

$$\|\mathbf{x}\|_N \equiv \left( \sum_{i=s+1}^{10} c_i^2 \right)^{1/2}, \quad (9)$$

where  $c_i$  is the  $i$ -th PC;  $s = 1$  in Fig. 2a and  $s = 2$  in Fig. 2b. The diagonal line indicates a signal-to-noise ratio of 1. If we take EOF-1 as the sole physical signal of zonal-mean flow variability, the majority of the data points fall into the upper triangle of Fig. 2a, where the signal-to-noise ratio is less than 1, and most of them are very close to the origin of the PC-1 axis.

On the other hand, if we retain the two leading EOFs as physical signal, as shown in Fig. 2b, the signal-to-noise ratio becomes substantially enhanced. Furthermore, many data points which previously lay near the climatological mean state viewed from PC-1 are now away from the origin.

[ Figure 2 near here, please ]

This result implies that if a PDF or histogram is computed using only PC-1, as in Akahori and Yoden (1997) or Hartmann and Lo (1998), a large fraction of the data points will fall near the origin, and any bimodality that might be present in the data could be obscured by noise [see also discussion in Mo and Ghil (1988) for NH regimes]. In order to avoid this situation, we proceed with PDF estimation in a two-dimensional (2-D) subspace spanned by the two leading EOFs. Including PC-3 in the “signal” does not change the data scatter in Fig. 2b substantially (not shown), so that we only retain the two leading EOFs.

As in Kimoto and Ghil (1993a) and Smyth et al. (1999), the PDF is estimated for a 2-D dataset, which consists of the projection coefficients of the unfiltered zonally and vertically averaged zonal wind anomalies onto the low-pass filtered EOFs shown in Fig. 1. Projecting the unfiltered data onto its own EOFs was found to yield a similar PDF but with a larger number of transient events. An adaptive version of the kernel method with the Epanechnikov kernel (Kimoto and Ghil 1993a) is used and Euclidean distance is employed as a similarity

measure. The adaptive method enables us to obtain more reliable density estimates in the data-sparse regions that lie on the outskirts of the PDF.

The smoothing parameter  $h$ , which controls the smoothness of final density estimates, needs to be properly specified. An objective way to determine this parameter is least-squares cross validation (LSCV), which minimizes an estimate of the integrated square error of the PDF fit (Silverman 1986). The LSCV scores are plotted as a function of the smoothing parameter  $h$  in Fig. 3. As is often the case in LSCV, the score has a fairly broad minimum, near  $h = 0.3$  and  $0.4$ . Both values result in similar estimates of the PDF.

[ Figure 3 near here, please ]

The PDF constructed with  $h = 0.4$  is displayed in Fig. 4a. The estimated PDF exhibits a pronounced central peak with two distinct shoulders attached to it. It is elongated along the PC-1 axis with a slight tilt toward the negative PC-2 axis.

[ Figure 4 near here, please ]

In order to establish the statistical significance of these three distinct features of the PDF, we generate one hundred random time series, of the same length as the original PC time series. These time series are based on a 2-D autoregressive process of order one (Wei 1990). More precisely, we consider a sequence of vectors  $\mathbf{X}_i$  that contain PC-1 and PC-2 of the dynamical model simulation at a given day  $i$ . This sequence satisfies

$$\mathbf{X}_{i+1} = \mathbf{A}\mathbf{X}_i + \mathbf{R}_i, \tag{10}$$

where  $\mathbf{A}$  is the correlation matrix at 1-day lag, while  $\mathbf{R}_i$  are the residuals. The two diagonal elements of  $\mathbf{A}$  are the autocorrelations and its two off-diagonal elements are the cross-correlations.

We want to compare the statistical properties of the sequence  $\mathbf{X}_i$ —generated by the dynamical model and having irregular residuals  $\mathbf{R}_i$ —with those of a sequence of centered random vectors  $\mathbf{Y}_i$  that have a bivariate normal distribution with zero mean and the same

lag-one correlation matrix as  $\mathbf{X}_i$ . The stochastic model that generates the sequence  $\mathbf{Y}_i$  is

$$\mathbf{Y}_{i+1} = \mathbf{A}\mathbf{Y}_i + \mathbf{W}_i. \quad (11)$$

The residuals of Eq. (11) are a Gaussian white-noise sequence  $\mathbf{W}_i$  that has zero mean

$$\langle \mathbf{W}_i \rangle = 0, \quad (12)$$

lag-one covariance zero, and lag-zero covariance

$$\langle \mathbf{W}_i \mathbf{W}_i^T \rangle = \langle \mathbf{R}_i \mathbf{R}_i^T \rangle; \quad (13)$$

the angle brackets denote time means and superscript  $T$  denotes transposition.

One hundred random PDFs are then computed from the 2-D random time series generated by the stochastic model (11)–(13), using the same kernel method with the same smoothing parameter  $h = 0.4$  as in Fig. 4a. The percentage of random PDFs so generated that fall short of the PDF values shown in Fig. 4a is plotted in Fig. 4b, with regions containing values that exceed 95 shaded. Both the peak and the shoulders in Fig. 4a are significant at the 95% confidence level. Although Fig. 4 does not show three distinct PDF peaks, it clearly indicates that there are three highly populated regions in phase space that deviate significantly from bivariate Gaussianity.

Probability density estimation, a major concern of this study, is solely based on the idea of the recurrence of particular flow patterns so that it does not, in principle, distinguish physically meaningful, quasi-steady, low-frequency phenomena from transient noise. As a result, transient noise that recurs frequently can also have high probability density and this may obscure inherent multiple regimes that might be present in the data. In order to examine this possibility, we consider a subset of the original data that represents quasi-stationary (QS) states.

First, the speed along the phase-space trajectory is computed for each day, using Euclidean distance between the two vectors two days apart in the 2-D phase plane shown in

Fig. 4. A centered difference scheme is used to compute the speed. We then select only QS days, whose speed lies below a prescribed value, taken to be the time mean minus one standard deviation. The resulting QS dataset consists of 4642 days. Note that the method described above is more conservative than Mo and Ghil’s (1987, 1988) use of pattern correlations to define slow change in the field of interest for a number of successive days, as shown by Vautard et al. (1988).

The PDF is estimated for this QS subset with the smoothing parameter  $h = 0.4$ , which is determined by the LSCV. The resulting PDF is shown in Fig. 5. Its general shape resembles Fig. 4a, but it exhibits three distinct PDF peaks, whose locations are very close to the peak and two shoulders in the PDF of the full dataset. This strongly suggests that the two shoulders are the trace of two distinct PDF peaks that exist inherently in the full data, but are obscured by transient noise.

[ Figure 5 near here, please ]

In order to corroborate further the evidence for the multiple regimes, we apply Gaussian mixture model clustering (Smyth et al. 1999) to the 2-D dataset used in the kernel density estimation. In this method, a PDF is assumed to be a linear combination of a few Gaussian component density functions, each with its own mean and covariance. Thus, a PDF can be multimodal in this generative sense, even if it exhibits only one distinct peak (Titterton et al. 1985). Unlike other clustering techniques, this method uses a consistent data-driven methodology based on cross-validated likelihood to estimate the number of clusters supported by the data.

First, we compute the cross-validated log-likelihood, following the procedures described in Smyth et al. (1999). Figure 6 shows the log-likelihood values against the number of clusters  $k$ . The likelihood curve exhibits a sharp increase from  $k = 1$  and then begins to saturate as  $k$  is increased further. The minimum at  $k = 1$  clearly indicates that a single Gaussian is most unlikely to represent the data PDF. When we increase the maximum

number of clusters from 6 to 10, the log-likelihood exhibits even more clearly the asymptotic nature of the saturation from  $k = 3$  on (not shown). This behavior suggests that we are experiencing the “overfitting” of a non-Gaussian PDF by an ever larger number of Gaussian clusters. A histogram of PC-1 (not shown) exhibits indeed deviations from Gaussianity, characterized by a lower central peak and shorter tails. We choose therefore  $k = 3$ , as the optimal trade-off between goodness-of-fit and statistical stability of the clusters’ centroids and other parameters. Indeed, the log-likelihood curve starts to flatten out at this value, which also agrees with the number of distinct peaks in Fig. 5.

[ Figure 6 near here, please ]

Given the number of clusters  $k = 3$ , we fit a three-component mixture model to the 2-D dataset used in the kernel density estimations. Figure 7 shows the location of the means of the Gaussians and the standard-deviation ellipses associated with their covariance matrices. The three ellipses agree with the general shape of the PDFs estimated by the kernel method, an arch shape elongated along the PC-1 axis. Two of the ellipses are mainly located on the positive and negative side of the PC-1 axis, respectively. The other ellipse is centered close to the origin with a slight shift toward the positive PC-1 and PC-2 axes.

[ Figure 7 near here, please ]

### *b. Physical characteristics of the regimes*

Having confirmed our kernel density estimation, we now construct regime composites in order to examine the physical-space picture associated with the three high-density regions in Fig. 4. First, the location of the regime centroids in phase space is found by using the bump-hunting algorithm of Fukunaga and Hostetler (1975). The resulting centroids are denoted by ‘+’ in Fig. 4a. These regime centroids in phase space are then converted to physical-space patterns, and pattern correlations between the centroids’ profiles and daily zonal-mean wind profiles are computed. We then identify recurrent *episodes* by collecting

into a given regime the days whose pattern correlation with the corresponding centroid is greater than 0.8. Finally, regime *events* are defined by taking recurrent episodes whose duration is equal to or longer than 6 days. Thus, regime events incorporate, by definition, recurrent and persistent patterns of zonal-mean flow.

Flow composites of the resulting regime events are shown in Fig. 8. They reveal three distinct anomalous zonal-jet states. In Regime 2, hereafter called the *low-latitude regime*, the jet is located equatorward of its climatological mean position, while in Regime 3, hereafter *high-latitude regime*, it is located poleward of this position. Finally, in Regime 1, the jet is strengthened near its climatological mean position. The low- and high-latitude regimes correspond to the shoulders near the positive and negative PC-1 axis in Fig. 4a, respectively. Thus, the composite anomalies of the two regimes reflect to a large extent the two opposite phases of EOF-1 in Fig. 1.

[ Figure 8 near here, please ]

Having identified multiple flow regimes, we investigate next the statistical properties of regime transitions. We adopt a Markov-chain description, following Ghil (1987), Mo and Ghil (1987, 1988), Vautard et al. (1990), and Kimoto and Ghil (1993b). First, we construct the transition matrix  $\mathbf{T}$ , whose element  $T_{ij}$  gives the number of transitions from regime  $i$  to  $j$ . Transition probability  $P_{ij}$  is estimated as  $P_{ij} = T_{ij}/n_i$ , where  $n_i$  is the total number of passages through regime  $i$ . The simulated dataset here is much longer than the observed datasets of the above-mentioned papers. This allows us to report actual transition probabilities  $P_{ij}$  as opposed to the previous reports of transition counts  $T_{ij}$  only.

Table 1 shows the estimated transition probability for all the regime episodes regardless of regime duration, as well as for regime events whose duration is of 6 days or longer. For both cases, the transition probability from the low- or high-latitude regime back to the regime itself is highest, while the probabilities of transition from Regime 1 (central-peak regime) to all three regimes (including itself) are fairly similar. Direct transitions between the low-

and high-latitude regimes, without passing through the centrally located regime, have non-negligible probabilities, regardless of the episodes' duration. The probability of transitions from the low- or high-latitude regime to Regime 1 is vanishingly small when only regime events are considered. It thus appears that Regimes 2 and 3, while associated with opposite polarities of EOF-1, are not just opposite phases of an oscillation in the jet's latitudinal position.

[ Table 1 near here, please ]

Although the regime composites in Fig. 8 might suggest a single zonal jet shifting meridionally, this impression is rather superficial and misleading. Careful inspection of the zonally and vertically averaged zonal flow on a daily basis reveals the occurrence of double jets during the high-latitude regime (not shown). These double jets are especially clear and more frequently observed at the upper level. Figure 9 shows the zonal-mean wind at each level composited with respect to the low- and high-latitude regime events.

[ Figure 9 near here, please ]

At the upper level, the high-latitude regime exhibits a broad profile with evidence of a double jet (Fig. 9b), while a single jet with strong meridional shear characterizes the low-latitude regime (Fig. 9a). Contrasts in vertical shear between the two regimes are also apparent in the figure. The role of the vertical and meridional shear shall be discussed in the next section. As evident from Fig. 9, the zonal-flow vacillation in our model is not characterized simply by the meridional displacement of a single jet, but by more complex changes in the meridional wind profile that are often associated (see also Table 1) with transitions between single- and double-jet states.

The regimes' persistence characteristics are summarized in Fig. 10 by plotting the number of recurrent episodes against their duration. The three straight lines indicate least-square linear fits to the data scatter for the three regimes. The number of recurrent episodes declines, in all three regimes, according to an approximate power law, i.e. the points for each

regime fall close to a straight line in the log-linear coordinates of Fig. 10. The situation for our zonally symmetric SH model regimes is thus similar to that recorded by Dole and Gordon (1983) and Kimoto and Ghil (1993b) for NH observations and by Legras and Ghil (1985) for their model’s zonally asymmetric regimes.

[ Figure 10 near here, please ]

In log-linear coordinates, the number of “runs” of a given duration—i.e., of times that a prescribed sign persisted for that duration or longer—is given by a straight line for a linear first-order Markov process with mean zero (Ghil and Childress 1987, pp. 181ff. and 323ff.). For example, consider the following linear first-order Markov process in continuous time:

$$\frac{du}{dt} = -\lambda u + \eta(t), \quad (14)$$

where  $u = u(t)$ ,  $\lambda$  is constant, and  $\eta$  represents Gaussian white noise with mean zero. By taking the ensemble mean,

$$\frac{d\langle u \rangle}{dt} = -\lambda \langle u \rangle, \quad (15)$$

and the solution  $\langle u \rangle = U(t)$  is given by

$$U(t) = u_o e^{-\lambda t}. \quad (16)$$

The “drift” or (negative) feedback coefficient  $-\lambda$  is the reciprocal of the process’s exponential relaxation time or  $e$ -folding time  $\tau = 1/\lambda$ . The value of  $\lambda$  can be estimated from the slope of the process’s persistence diagram when plotted in log-linear coordinates, as done in Fig. 10.

The  $e$ -folding times for the three regimes are estimated from the straight regression lines shown in Fig. 10. For Regime 1 the estimate is  $\tau = 3.6$  days, while the low- and high-latitude regimes have  $\tau = 13.0$  and 14.1 days, respectively. As evident from this, the central-peak regime is about three times less persistent than the other two regimes. Hereafter, we focus only on the two more persistent regimes that characterize zonal-flow vacillation.



## 4 Time evolution of zonal-flow vacillation

### *a. Model diagnostics and compositing procedures*

The essence of zonal-flow vacillation can be described in the quasi-geostrophic, zonally averaged equations on a  $\beta$ -plane:

$$\frac{\partial \bar{u}}{\partial t} = f_0 \bar{v} - \frac{\partial}{\partial y} (\overline{u'v'}) + \bar{F}, \quad (17)$$

$$\frac{\partial \bar{\theta}}{\partial t} = -\bar{\omega} \frac{\partial \Theta}{\partial p} - \frac{\partial}{\partial y} (\overline{v'\theta'}) + \bar{Q}, \quad (18)$$

$$f_0 \frac{\partial \bar{u}}{\partial p} = \hat{R} \frac{\partial \bar{\theta}}{\partial y}, \quad (19)$$

where an overbar denotes a zonal average and a prime indicates a deviation from the zonal average. The zonal-average mechanical forcing  $\bar{F}$  is dominated by surface friction [see Eq. (6)];  $\bar{Q}$  is the zonal-average thermal forcing [Eq. (7)],  $\Theta = \Theta(p)$  the reference potential temperature, and  $\hat{R} = (p/p_0)^\kappa R/p$  the normalized gas constant.

For a given mechanical forcing  $\bar{F}$ , the zonal momentum Eq. (17) states that zonal wind is driven by the Coriolis acceleration due to meridional motion and by the meridional convergence of westerly eddy momentum flux. If Eq. (17) is vertically averaged using the upper and lower boundary conditions, the Coriolis acceleration term vanishes and the eddy momentum flux convergence becomes the only driving forcing of the zonal-flow vacillation against the frictional drag. For a given thermal forcing  $\bar{Q}$ , potential temperature is controlled by two competing terms in the thermodynamic Eq. (18): the adiabatic cooling/heating term associated with vertical motion and the eddy heat flux convergence/divergence term due to meridional temperature advection by eddies. The thermal-wind Eq. (19) links the dynamics governed by Eq. (17) and the thermodynamics controlled by Eq. (18). Equations (17)–(19) are now used to examine the dynamics of the low- and high-latitude regimes.

In order to investigate the time evolution of the model’s zonal-flow vacillation, composites for the two extreme phases of the vacillation were constructed. First, days belonging to either a low- or high-latitude regime event are numbered consecutively, e.g.  $[1, 2, \dots, n]$ , and then normalized to constitute a closed time interval of  $[0, 10]$ . The choice of this standardized event duration of 10 days is motivated by the average durations of the low- and high-latitude regime events, which are 10.2 and 10.1 days, respectively. The days corresponding to the standardized times  $t = 0$  and  $t = 10$  days are defined to constitute the regime’s onset and break, respectively. The actual data points within the standardized time interval  $[0, 10]$  are interpolated for each event to 11 equidistant points, using cubic spline interpolation. Note that the actual signals at regime onset and break are not affected by this interpolation.

We now collect days before the onset and after the break, selecting the same number of days before and after as the duration of the specific regime event itself. The same normalization and interpolation techniques are applied to these two time intervals on either side of the regime, resulting in the standardized time intervals of  $[-10, 0]$  and  $[10, 20]$ . By combining these three intervals, we have the temporal evolution of a regime event for the normalized time interval  $[-10, 20]$  with increments of 1.

The above procedures are repeated for all 277 and 289 events of the low- and high-latitude regimes, respectively. Composites of key physical variables are made for these events with respect to the standardized time interval of  $[-10, 20]$ . In the following subsection, we only show the interval  $[-4, 14]$  for clarity. The method described above provides a very compact view of the entire evolution of the regimes, from onset to break, in a single figure. In contrast to the middle-day composites used by Feldstein and Lee (1996), our method does not smear out the signals associated with regime onset and break.

### *b. Onset, maintenance, and break*

Figure 11 shows anomaly composites of key variables with respect to standardized regime

evolution for the low- (left panels) and high-latitude (right panels) regimes. Shaded regions are statistically significant at the 95% level by a two-sided pointwise  $t$ -test. Panels (a) and (b) show the vertically averaged zonal mean wind and clearly demonstrate the dipolar nature of the zonal-flow variability centered at  $40^\circ$  and  $60^\circ$ , consistent with Fig. 8b and previous SH observations. The low-latitude regime exhibits less variability within the regime itself than the high-latitude regime, resulting in a near steady state.

[ Figure 11 near here, please ]

In order to measure the rate of changes in the zonal-wind profile shown in Figs. 11a and 11b, we compute the root-mean-square (RMS) difference between two meridional profiles two days apart, using a centered difference scheme, and divide it by the time interval elapsed. The quantity so obtained is a measure of the acceleration (or deceleration) of the zonal mean wind, and equivalent to the speed along the model's phase-space trajectory [see Legras and Ghil (1985) for a NH model and Vautard (1990) for NH observations]. The composites of this acceleration with respect to standardized regime evolution are shown in Fig. 12.

[ Figure 12 near here, please ]

A similar picture (not shown) is obtained by compositing the phase-space trajectory's speed, in the 2-D phase plane spanned by the projection coefficients of the two leading EOFs shown in Fig. 1. This similarity bears out further the fact that the two leading principal components do indeed constitute the signal, as suggested by the results in Fig. 2.

During the regime maintenance phase, the low-latitude regime exhibits a lower RMS acceleration than the high-latitude regime. This is consistent with Figs. 11a and 11b, which show less variability within the low-latitude regime than the high-latitude regime.

Abrupt onsets are clearly observed for both the low- and high-latitude regimes. On the other hand, the regime break shows an interesting asymmetry: a slower change is observed for the low-latitude regime while an abrupt break is clear for the high-latitude regime.

The statistical significance of the asymmetry between the breaks of the low- and high-

latitude regimes is tested in the following way. First, we collect the RMS zonal-wind acceleration of the 277 low-latitude regime breaks and the 289 high-latitude regime breaks. The 566 samples are then randomly shuffled one hundred times. For each random shuffling, composites of 277 and 289 samples are computed, resulting in 100 sets of the sample means. Finally, the lower 5% and upper 95% values of these 100 sets are compared with the composites of the RMS accelerations associated with the low- and high-latitude regime breaks. The asymmetry between the breaks of the two regimes is found to be significant at the 95% level. Similarly, the asymmetry between the onset and the break of the low-latitude regime is also found to be significant at the 95% level.

Figures 11c and 11d depict the vertical shear of the zonal mean wind, which is closely related to the horizontal temperature gradient through the thermal-wind balance. The anomalies near  $40^\circ$  and  $60^\circ$ , which correspond to zones of anomalous baroclinicity, are roughly in phase with the anomalies in the vertically averaged zonal mean wind. Panels (e) and (f) of Fig. 11 show anomalies of vertically averaged eddy momentum flux convergence, i.e. the forcing of the zonal mean wind [see Eq. (17)]. The in-phase nature of the barotropic zonal mean wind anomalies and the eddy momentum flux convergence demonstrates that the eddy momentum forcing acts to maintain the anomalous position of the jet against surface friction, consistent with previous studies (Robinson 1991; Yu and Hartmann 1993; Hartmann and Lo 1998).

At the time of regime onset, anomalously strong eddy momentum forcing is observed for both regimes, consistent with the abrupt changes in zonal-mean flow observed in Fig. 12. Eddy momentum forcing near break exhibits an asymmetry between the low- and high-latitude regimes. In the case of the low-latitude regime, the eddy momentum forcing anomalies become very small near the break, consistent with the low RMS zonal-wind acceleration at the break shown in Fig. 12. The high-latitude regime break, on the other hand, is accompanied by a poleward shift of the negative eddy momentum forcing anomalies from the

mid-latitudes. This feature is associated with the more rapid termination of the high-latitude regime.

Panels (g) and (h) of Fig. 11 show the low-level eddy heat flux. Prior to regime onset, strong positive anomalies in the eddy heat flux are observed at the central latitudes of both regimes. They are followed by eddy momentum forcing anomalies (Figs. 11e and 11f) and thus by abrupt acceleration of zonal mean wind anomalies at the time of regime onset (Fig. 12). This demonstrates the baroclinic nature of the eddies that drive the zonal-mean wind anomalies. The temporal lag between the evolution of the eddy heat flux and the eddy momentum flux convergence, on the one hand, and the near-simultaneous occurrence of changes in the eddy momentum forcing and zonal wind acceleration, on the other, are consistent with the dynamical picture suggested by the studies discussed in Section 1. In this picture, equatorward propagation of baroclinic eddies and subsequent eddy mean-flow interactions lead to eddy momentum forcing that accelerates the upper-level zonal-mean flow.

As mentioned in Section 1, it is now recognized that the persistence of zonal wind anomalies during the extreme phases of the vacillation is due to the reinforcement of the anomalous zonal flow by the convergence of transient eddy momentum fluxes. In the context of the model regimes, the idealized feedback argument runs as follows: upon an initial eddy momentum forcing, the zonal-mean wind starts to accelerate near  $40^\circ$  and  $60^\circ$  for the low- and high-latitude regime, respectively. The stronger eddy momentum forcing at the upper level and the deceleration of the low-level flow by surface friction lead to differential acceleration in the vertical. The enhanced vertical shear feeds baroclinic instability that generates baroclinic eddies. The resulting eddies propagate preferentially equatorward due to the sphericity of the earth, and associated eddy zonal-mean flow interactions lead to an eddy momentum flux convergence at the upper level, closing the feedback loop.

The low-level eddy heat flux in Figs. 11g and 11h shows a distinct asymmetry between the

low- and high-latitude regime. The low-latitude regime displays dipolar anomalies centered at  $40^\circ$  and  $60^\circ$ . The positive eddy heat flux anomalies along  $40^\circ$  persist until standardized time  $t = 7$  days, at which time they begin to attenuate (Fig. 11g); this is consistent with a similar behavior of the eddy momentum forcing at  $40^\circ$  (Fig. 11e). The high-latitude regime, on the other hand, shows very weak positive anomalies at  $60^\circ$  throughout the event, while strong negative anomalies dominate in mid-latitudes (Fig. 11h). These negative anomalies extend poleward, nearly up to  $60^\circ$ , and increase in magnitude until the regime break; this is consistent with the poleward shift in eddy momentum forcing near the high-latitude regime break (Fig. 11f). For both the low- and high-latitude regimes, the changes in the low-level eddy heat flux near the regime break (Figs. 11g and 11h) precede those of eddy momentum forcing (Figs. 11e and 11f) by one normalized day or so, as in the case for the regime onset.

We next examine the dynamics of the vacillation in terms of energetics averaged over the mid-latitude region, i.e. approximately  $25^\circ$ – $65^\circ$ . First, the energetics are calculated from the daily data, based on the quasi-geostrophic formalism of Randel and Stanford (1985). We then composite the energetics with respect to the standardized regime evolution, as in Figs. 11 and 12. Composite anomalies in zonal-mean available potential energy (APE) and total eddy energy, which consists of eddy APE and eddy kinetic energy (KE), and zonal-mean KE are shown in Figs. 13a–c, respectively. Separate composites of the eddy APE and eddy KE (not shown) are found to be similar. We repeated the energetics calculations for a wider domain, of approximately  $20^\circ$ – $70^\circ$ , and the results (not shown) are very similar to those in Fig. 13.

[ Figure 13 near here, please ]

The zonal mean APE increases during the low-latitude regime, while it decreases during the high-latitude regime (Fig. 13a). This difference in behavior is due to the different time evolution of zonal mean temperature (not shown) that determines the zonal mean APE. In contrast to the zonal mean APE, the total eddy energy shows a consistent decrease for

both regimes, from onset till break, although the decrease is more pronounced for the high-latitude regime (Fig. 13b). The zonal-mean KE displays a similar temporal evolution for both regimes, with an initial increase just before the onset, followed by a decrease that lasts throughout the regime and past its break (Fig. 13c). Again, the decrease is steeper for the high-latitude regime.

The peculiar feature that the total eddy energy decreases during the low-latitude regime despite the increase in zonal mean APE is reminiscent of the effect of the “barotropic governor.” James and Gray (1986) noted that numerical simulations with reduced bottom drag develop strong horizontal shear that inhibits baroclinic instability and thus baroclinic energy conversion; they called this effect of horizontal shear the barotropic governor. Linear stability analysis has been used to demonstrate that barotropic shear in the mean flow can prevent the optimal growth of baroclinic waves by reducing their meridional coherence, and thus reduce the growth of eddy energy (James 1987; Nakamura 1993a).

Our low-latitude regime does, indeed, possess strong meridional shear in mid-latitudes, due to the development of a strong single jet (Figs. 8a and 9a). The emergence of the strong jet at the low-latitude regime’s onset (see also Fig. 11a) explains the sharp initial increase in zonal-mean KE (Fig. 13c). The subsequent decrease in zonal-mean KE may be attributed to the decrease in total eddy energy; the latter, in turn, may be due to the effect of the barotropic governor. The fact that the high-latitude regime is characterized by a broad jet with weak meridional shear (see Figs. 8a and 9b) suggests that the effect of the barotropic governor in this case might be smaller. In the absence of other mechanisms, the decrease in zonal-mean APE could be the cause of the decrease in both total eddy energy and zonal-mean KE during the high-latitude regime.

## 5 Dependence on surface friction

Surface friction plays an important role in regime maintenance, balancing anomalous eddy momentum forcing [see Eq. (17)]. In order to examine further the influence of surface friction

on zonal-flow vacillation, six additional runs were carried out, all having the same length of 30000 days as the control run. All parameter values were held fixed in the seven runs except for the Ekman drag time scale  $\tau_E$ , which controls the strength of the frictional bottom drag [see Eq. (6)]. The seven values of  $\tau_E$  were 1.0, 1.5, 2.0, 2.5, 3.0 (control), 4.0 and 8.0 days.

Bivariate PDFs of the zonally and vertically averaged zonal-wind profiles were constructed for each of the seven runs, as described in Section 3. The precise locations of the peaks and shoulders were obtained using the bump-hunting algorithm, in the subspace of the two leading EOFs. Depending on the parameter value  $\tau_E$ , we identified one, two or three zonal-flow regimes. As in Section 3, data points that have pattern correlations of 0.8 or higher with the regime centroids in physical space were collected, and the corresponding composite profiles of zonally and vertically averaged zonal wind were computed.

The resulting latitudinal positions of the zonal-jet maxima are plotted relative to the reciprocal Ekman drag time scale  $1/\tau_E$  in Fig. 14. For an intermediate range of bottom-friction values of 1.5 days  $\leq \tau_E \leq 4$  days, multiple zonal-jet regimes coexist. The zonal jet's latitudinal position and its intensity jump irregularly from one regime to another within this range. For the smallest or largest values of surface drag, only one zonal-jet regime obtains. This is consistent with Akahori and Yoden's (1997) result that the bimodality of their LC index depends on the surface drag.

[ Figure 14 near here, please ]

Surface friction is found to have a substantial impact on the zonal-mean flow. The run using the lowest drag (highest value of  $\tau_E$ ) exhibits stronger and more agitated flows than the control run. This explains the decreased power in the ultra low-frequency band (period  $T > 60$  days) and the increased power in the higher-frequency band of the zonal flow's power spectrum (not shown). Overall, lower drag values yield zonal jets that are displaced further poleward. Robinson (1997) showed that this poleward shift of the barotropic jet is due to the changes in the meridional structure of the eddy momentum fluxes that force it.



On the other hand, the highest-drag run shows weaker flows with reduced high-frequency variability and enhanced low-frequency variability of the zonal-mean flow. This is consistent with Robinson’s (1996) result that the enhanced baroclinicity due to increased surface drag leads to more persistent zonal jets. These jets arise from the stronger feedback between the high-frequency eddies and the zonal-mean flow.

## 6 Concluding remarks

### *a. Multiple regimes and their key properties*

In the present paper, we have investigated zonal-flow vacillation in a two-layer global primitive equation model. This vacillation is characterized by irregular meridional fluctuations of the zonal jet. In spite of its high degree of idealization, our model simulates well the observed meridional structure of zonal-flow variability in the SH, with equivalent-barotropic anomalies of opposite signs centered at  $40^\circ$  and  $60^\circ$ .

Motivated by previous studies of multiple regimes, we have applied two advanced density estimation techniques, the kernel method and Gaussian mixtures, to model simulations of the zonally and vertically averaged zonal wind. In order to obtain results with high statistical significance, simulations that are 30000 days long were used. We estimated a Euclidean PDF by the kernel method in the phase subspace spanned by the two leading EOFs of the zonal wind field, and found it to exhibit multiple regimes. These regimes were identified as a pronounced central peak with two distinct “shoulders” attached to it (Fig. 4); all three features are statistically significant at the 95% confidence level against a null hypothesis of bivariate red noise. A quasi-stationary (QS) data subset, which includes only days with slower speeds of the phase-space trajectory, exhibits three distinct PDF peaks, confirming the existence of multiple regimes (Fig. 5). The Gaussian mixture model clearly indicates that a single Gaussian is extremely unlikely to represent the PDF of the data, and supports

the evidence for three distinct regimes (Figs. 6 and 7).

Flow composites associated with the regime centroids capture three distinct zonal-jet states. A strong jet near its climatological mean position is associated with the central peak in the PDF. The two PDF shoulders (or additional peaks, depending on the dataset and estimation method) have the jet maximum located equatorward (*low-latitude regime*) or poleward (*high-latitude regime*) of its climatological position. The high-latitude regime is found to be associated with a double jet at the upper level, while the low-latitude regime is characterized by a strong single jet with enhanced meridional shear (Figs. 8 and 9). This asymmetry in jet structure suggests that zonal-flow vacillation does not simply involve meridional shifts in the jet’s position and changes in its intensity.

Given the length of our model simulations, we were able to compute transition probabilities between regimes (Table 1). The transition matrix supports the idea—already emerging from the asymmetry of the jet structure in the two off-climatology regimes—that the vacillation is not a manifestation of linear oscillations about the climatological mean jet. Indeed, this matrix shows that direct transitions between the low- and high-latitude regimes, without passing through the central-peak regime, are fairly likely. Furthermore, the duration of passages through the two extreme regimes is about three times as long as that through the near-climatology regime.

As discussed in Section 1, bimodality or multiple regimes in zonal-mean flow were found neither by Akahori and Yoden (1997) in a simple global circulation model nor by Hartmann and Lo (1998) in SH observations. This major difference between their results and ours appears to be due to the fact that we performed our analysis in a 2-D phase subspace while previous studies relied on one-dimensional (1-D) histograms. Our analysis of the signal-to-noise ratio in the model simulation (Fig. 2) amply justifies the choice of the 2-D subspace spanned by the two leading EOFs. We performed a similar PDF estimation in a 1-D subspace using PC-1 and did not find strong evidence of either bimodality or multiple regimes. Mo

and Ghil (1988) also showed that inhomogeneity of a PDF, i.e. deviations from Gaussianity, can be detected more easily in a multi-dimensional space than in 1-D space. This is because the peaks and shoulders of the PDF are not necessarily located on the PC-1 axis, as shown in Fig. 4a (see also Kimoto and Ghil 1993a).

### *b. Standardized evolution of regime events*

To investigate the temporal evolution of the vacillating zonal jet we restricted our attention to regime *events*, i.e. to low- or high-latitude episodes that last 6 days or longer. For the purpose of compositing, the duration of each such event was normalized to 10 days, from onset at  $t = 0$  to break at  $t = 10$ ; the number of days before onset and after break that equals a specific event’s duration was normalized in the same way. The composite evolution of various quantities was then plotted on this standardized  $[-10, 20]$  interval (Figs. 11–13), showing only the results for  $[-4, 14]$ .

Both regimes’ onsets are found to be abrupt (Fig. 12). The breaks, however, show a significant asymmetry between the two regimes: an abrupt break is evident for the high-latitude regime, while it is more gradual for the low-latitude regime. The eddy momentum flux convergence that forces the zonal-mean flow exhibits a similar asymmetry between the two regime breaks (Figs. 11e and 11f). The low-latitude regime break is caused by a “turn-off” of the existing forcing at the key latitude  $40^\circ$  (Fig. 11e), while the high-latitude regime break is driven by the shift of negative forcing anomalies from  $40^\circ$  to  $50^\circ$  (Fig. 11f).

The asymmetry between the regime breaks is somewhat reminiscent of the concept of a NH zonal-index cycle (Rossby and Willett 1948; Namias 1950). These authors described the index cycle as a relaxation oscillation, with slow transitions from low to high index and fast transitions from high to low index. Willett (1948) found that the low- and high-index phases of the NH jet are associated with latitudinal shifts of the jet as well as changes in its intensity. Thus, they would correspond, very roughly, to our low- and high-latitude

regimes, respectively. Although the importance of the index cycle in the NH has been criticized (e.g. Wallace and Hsu 1985), there has been a recent resurgence of interest in the zonally symmetric mode of variability in the NH (Thompson and Wallace 2000; Thompson et al. 2000). Wallace (2000) has drawn further attention to the connections between a zonally symmetric seesaw or “annular mode” [see also Mo and Ghil’s (1988) “North-South oscillation,” their Fig. 10d] and the North Atlantic Oscillation [see also the sectorial and hemispheric features of Keppenne et al.’s (2000) 70-day oscillation].

Consistent with previous studies, we found that baroclinic eddies act to maintain the zonal-flow regimes via weakening or strengthening of the poleward transfer of westerly momentum from lower latitudes. The high correlation between the zonal-wind anomalies and the eddy momentum forcing anomalies suggests a substantial feedback between the two. The eddy momentum forcing at regime onset is preceded by anomalous low-level eddy heat flux, consistent with previous studies (Lee and Feldstein 1996; Feldstein and Lee 1996; Robinson 2000). Eddy heat flux changes lead those in eddy momentum flux convergence by about 1 or 2 normalized days, while changes in eddy momentum forcing and zonal wind acceleration occur simultaneously.

These lead-lag relationships are consistent with a dynamical picture in which equatorward propagation of baroclinic eddies and subsequent eddy mean-flow interactions lead to eddy momentum forcing that accelerates the upper-level zonal-mean flow. Changes in the low-level eddy heat flux near regime break also precede those of the eddy momentum forcing, as in the case of the regime onset. Baroclinic processes appear thus to be important for both regime onset and regime break.

The strong meridional shear and consistent decrease in eddy energy during low-latitude regime events suggest that the “barotropic governor” effect is active: horizontal shear tends to prevent the growth of baroclinic eddies by reducing their meridional coherence and thus leads to a reduction in the growth of eddy energy. The barotropic governor may also be

responsible for the weakening of positive eddy heat flux anomalies at  $40^\circ$  near the low-latitude regime break. The effect of the horizontal shear is strongest in an inviscid environment, in which most previous studies were conducted (James and Gray 1986; James 1987; Nakamura 1993b).

When surface friction is present, as it is in our model, the barotropic shear competes against the baroclinic shear that tends to maintain the generation of baroclinic eddies through the positive feedback between the eddies and zonal-mean flow. Our results suggest, therefore, that surface friction and the barotropic-governor effect play a major role in the gradual break of the low-latitude regime.

Depending on the strength of bottom friction, we found one, two or three zonal-flow regimes, with multiple regimes present for the Ekman drag time scale  $\tau_E$  between 1.5 and 4.0 days (Fig. 14). In this parameter range, the time evolution of the zonal jet is characterized by irregular jumps from one regime to another. Model simulations that used higher drag values tend to exhibit reduced high-frequency variability of zonal jets. This is consistent with Robinson’s (1996) conclusion that the enhanced baroclinicity due to increased surface drag leads to more persistent zonal jets as the feedback between the high-frequency eddies and the zonal flow becomes stronger. Overall, lower-drag runs yield stronger zonal jets that are displaced further poleward.

The dependence of flow regime on bottom drag and the coexistence of multiple regimes in Fig. 14 is somewhat reminiscent of the *S*-shaped bifurcation curves that arise from back-to-back saddle-node bifurcations [e.g., Figs. 6.5 and 10.6 in Ghil and Childress (1987)]. The details of the bifurcations, if indeed present, remain to be worked out, along with the stability of the distinct branches that arise from them.

Multiple regimes associated with vacillating zonal flow do coexist in our idealized primitive-equation model. The existence of multiple regimes in the SH’s zonal-mean flow, however, is still subject to debate. It is also interesting to note that the multiple regimes found in

our model cannot be explained by the theories of multiple flow equilibria that emphasize the role of topography (Charney and DeVore 1979; Charney and Straus 1980; Reinhold and Pierrehumbert 1982; Benzi et al. 1986; Ghil and Childress 1987, Ch. 6). Further investigations, based on observational as well as on hierarchical modeling studies (Ghil and Robertson 2000), are required to resolve the remaining questions raised in this discussion of our results.

*Acknowledgments.* We would like to thank Dr. R. Saravanan for providing his atmospheric model, which became the basis of the model used in this study. Fruitful discussions with Drs. M. Kimoto, K. Ide and S. Feldstein are gratefully acknowledged. The manuscript benefited substantially from careful reviews by W. Robinson and two anonymous reviewers. This research was supported by the University of California's Campus Laboratory Collaboration (CLC) program (SK), DOE Grant DE-FG03-98ER62615 (AWR) and NASA grant NAG 5-713 (MG). This is publication number 5387 of UCLA's Institute of Geophysics and Planetary Physics.

## References

- Akahori, K. and S. Yoden, 1997: Zonal flow vacillation and bimodality of baroclinic eddy life cycles in a simple global circulation model. *J. Atmos. Sci.*, **54**, 2349–2361.
- Benzi, R., A. Speranza, and A. Sutera, 1986: A minimal baroclinic model for the statistical properties of low-frequency variability. *J. Atmos. Sci.*, **43**, 2962–2967.
- Charney, J. G. and J. G. DeVore, 1979: Multiple flow equilibria in the atmosphere and blocking. *J. Atmos. Sci.*, **36**, 1205–1216.
- Charney, J. G. and D. M. Straus, 1980: Form-drag instability, multiple equilibria and propagating planetary waves in baroclinic, orographically forced, planetary wave systems. *J. Atmos. Sci.*, **37**, 1157–1176.
- Cheng, X. and J. M. Wallace, 1993: Cluster analysis of the Northern Hemisphere wintertime 500-hPa height field: Spatial patterns. *J. Atmos. Sci.*, **50**, 2674–2696.
- Dole, R. M. and N. D. Gordon, 1983: Persistent anomalies of the extratropical Northern Hemisphere wintertime circulation: Geographical distribution and regional persistent characteristics. *Mon. Wea. Rev.*, **111**, 1567–1586.
- Feldstein, S. and S. Lee, 1996: Mechanisms of zonal index variability in an aquaplanet GCM. *J. Atmos. Sci.*, **53**, 3541–3555.
- Feldstein, S. and S. Lee, 1998: Is the atmospheric zonal index driven by an eddy feedback? *J. Atmos. Sci.*, **55**, 3077–3086.
- Fukunaga, K. and L. D. Hostetler, 1975: The estimation of the gradient of a density function. *IEEE Trans. Info. Thy.*, **IT-21**, 32–40.
- Ghil, M., 1987: Dynamics, statistics, and predictability of planetary flow regimes. In C. Nicolis and G. Nicolis (Eds.), *Irreversible Phenomena and Dynamical Systems Analysis in the Geosciences*. D. Reidel. pp. 241–283.

- Ghil, M. and S. Childress, 1987: *Topics in Geophysical Fluid Dynamics: Atmospheric Dynamics, Dynamo Theory, and Climate Dynamics*. Springer-Verlag. 485 pp.
- Ghil, M. and A. W. Robertson, 2000: Solving problems with GCMs: General Circulation Models and their role in the climate modeling hierarchy. In D. Randall (Ed.), *General Circulation Model Development: Past, Present, and Future*. Academic Press. pp. 285–325.
- Ghil, M. and R. Todling, 1996: Tracking atmospheric instabilities with the Kalman filter. 2. Two-layer results. *Mon. Wea. Rev.*, **124**, 2340–2352.
- Hansen, A. R. and A. Sutera, 1986: On the probability density distribution of planetary-scale atmospheric wave amplitude. *J. Atmos. Sci.*, **43**, 3250–3265.
- Hartmann, D. L. and F. Lo, 1998: Wave-driven zonal flow vacillation in the Southern Hemisphere. *J. Atmos. Sci.*, **55**, 1303–1315.
- Hendon, H. H. and D. L. Hartmann, 1985: Variability in a nonlinear model of the atmosphere with zonally symmetric forcing. *J. Atmos. Sci.*, **42**, 2783–2797.
- James, I. N., 1987: Suppression of baroclinic instability in horizontally sheared flows. *J. Atmos. Sci.*, **44**, 3710–3720.
- James, I. N. and L. J. Gray, 1986: Concerning the effect of surface drag on the circulation of a baroclinic planetary atmosphere. *Quart. J. R. Met. Soc.*, **112**, 1231–1250.
- Keppenne, C. L., S. L. Marcus, M. Kimoto, and M. Ghil, 2000: Intraseasonal variability in a two-layer model and observations. *J. Atmos. Sci.*, **57**, 1010–1028.
- Kidson, J. W., 1988: Indices of the Southern Hemisphere zonal wind. *J. Climate*, **1**, 183–194.
- Kimoto, M. and M. Ghil, 1993a: Multiple flow regimes in the Northern Hemisphere winter. Part I: Methodology and hemispheric regimes. *J. Atmos. Sci.*, **50**, 2625–2643.



- Kimoto, M. and M. Ghil, 1993b: Multiple flow regimes in the Northern Hemisphere winter. Part II: Sectorial regimes and preferred transitions. *J. Atmos. Sci.*, **50**, 2645–2673.
- Lee, S. and S. Feldstein, 1996: Mechanism of zonal index evolution in a two-layer model. *J. Atmos. Sci.*, **53**, 2232–2246.
- Legras, B. and M. Ghil, 1985: Persistent anomalies, blocking and variations in atmospheric predictability. *J. Atmos. Sci.*, **42**, 433–471.
- Lorenz, E. N., 1960: Energy and numerical weather prediction. *Tellus*, **12**, 364–373.
- Mechoso, C., J. Farrara, and M. Ghil, 1991: Intraseasonal variability of the winter circulation in the Southern Hemisphere atmosphere. *J. Atmos. Sci.*, **48**, 1387–1404.
- Michelangeli, P.-A., R. Vautard, and B. Legras, 1995: Weather regimes: Recurrence and quasi stationarity. *J. Atmos. Sci.*, **52**, 1237–1256.
- Mo, K. C. and M. Ghil, 1987: Statistics and dynamics of persistent anomalies. *J. Atmos. Sci.*, **44**, 877–901.
- Mo, K. C. and M. Ghil, 1988: Cluster analysis of multiple planetary flow regimes. *J. Geophys. Res.*, **93**, 10927–10952.
- Nakamura, N., 1993a: An illustrative model of instabilities in meridionally and vertically sheared flows. *J. Atmos. Sci.*, **50**, 357–375.
- Nakamura, N., 1993b: Momentum flux, flow symmetry, and the nonlinear barotropic governor. *J. Atmos. Sci.*, **50**, 2159–2179.
- Namias, J., 1950: The index cycle and its role in the general circulation. *J. Meteor.*, **7**, 130–139.
- Randel, W. J. and J. L. Stanford, 1985: An observational study of medium-scale wave dynamics in the Southern Hemisphere summer. Part I: Wave structure and energetics. *J. Atmos. Sci.*, **42**, 1172–1188.

- Reinhold, B. B. and R. T. Pierrehumbert, 1982: Dynamics of weather regimes: Quasi-stationary waves and blocking. *Mon. Wea. Rev.*, **110**, 1105–1145.
- Robinson, W. A., 1991: The dynamics of the zonal index in a simple model of the atmosphere. *Tellus*, **43A**, 295–305.
- Robinson, W. A., 1996: Does eddy feedback sustain variability in the zonal index? *J. Atmos. Sci.*, **53**, 3556–3569.
- Robinson, W. A., 1997: Dissipation dependence of the jet latitude. *J. Climate*, **2**, 176–182.
- Robinson, W. A., 2000: A baroclinic mechanism for the eddy feedback on the zonal index. *J. Atmos. Sci.*, **57**, 415–422.
- Rossby, C.-G. and H. C. Willett, 1948: The circulation of the upper troposphere and lower stratosphere. *Science*, **108**, 643–652.
- Saravanan, R. and J. C. McWilliams, 1995: Multiple equilibria, natural variability, and climate transitions in an idealized ocean-atmosphere model. *J. Climate*, **8**, 2296–2323.
- Silverman, B. W., 1986: *Density Estimation for Statistics and Data Analysis*. Chapman and Hall. 175 pp.
- Smyth, P., K. Ide, and M. Ghil, 1999: Multiple regimes in Northern Hemisphere height fields via mixture model clustering. *J. Atmos. Sci.*, **56**, 3704–3723.
- Thompson, D. W. J. and J. M. Wallace, 2000: Annular modes in the extratropical circulation. Part I: Month-to-month variability. *J. Climate*, **13**, 1000–1016.
- Thompson, D. W. J., J. M. Wallace, and G. C. Hegerl, 2000: Annular modes in the extratropical circulation. Part II: Trends. *J. Climate*, **13**, 1018–1036.
- Titterton, D. M., A. F. M. Smith, and U. E. Makov, 1985: *Statistical Analysis of Finite Mixture Distributions*. John Wiley and Sons. 243 pp.

- Trenberth, K. E., 1979: Interannual variability of the 500-mb zonal mean flow in the Southern Hemisphere. *Mon. Wea. Rev.*, **107**, 1515–1524.
- Vautard, R., 1990: Multiple weather regimes over the North Atlantic: Analysis of precursors and successors. *Mon. Wea. Rev.*, **118**, 2056–2081.
- Vautard, R., B. Legras, and M. Déqué, 1988: On the source of midlatitude low-frequency variability. Part I: A statistical approach to persistence. *J. Atmos. Sci.*, **45**, 2811–2843.
- Vautard, R., K. C. Mo, and M. Ghil, 1990: Statistical significance test for transition matrices of atmospheric Markov chains. *J. Atmos. Sci.*, **47**, 1926–1931.
- Wallace, J. M., 2000: North Atlantic Oscillation/annular mode: Two paradigms—one phenomenon. *Quart. J. R. Met. Soc.*, **126**, 791–805.
- Wallace, J. M. and H. H. Hsu, 1985: Another look at the index cycle. *Tellus*, **37A**, 478–486.
- Webster, P. J. and J. L. Keller, 1975: Atmospheric variations: vacillations and index cycles. *J. Atmos. Sci.*, **32**, 1283–1300.
- Wei, W. W. S., 1990: *Time Series Analysis*. Addison Wesley. 478 pp.
- Willett, H. C., 1948: Patterns of world weather changes. *Trans. Amer. Geophys. Union*, **29**, 803–809.
- Yoden, S., M. Shiotani, and I. Hirota, 1987: Multiple planetary flow regimes in the Southern Hemisphere. *J. Meteor. Soc. Japan*, **65**, 571–585.
- Yu, J.-Y. and D. L. Hartmann, 1993: Zonal flow vacillation and eddy forcing in a simple GCM of the atmosphere. *J. Atmos. Sci.*, **50**, 3244–3259.

# List of Figures

1	The two leading EOFs of the 10-day low-pass filtered zonally and vertically averaged zonal flow. . . . .	40
2	Data scatter in terms of leading EOFs. (a) Abscissa is the root-mean square (RMS) magnitude of anomalies in phase space computed with only PC-1, and ordinate is the RMS magnitude of anomalies with PC-2 through PC-10. (b) Abscissa is the RMS magnitude of anomalies computed with PC-1 and PC-2, and ordinate is the RMS magnitude of anomalies with PC-3 through PC-10. . . . .	41
3	Least-squares cross validation (LSCV) scores as a function of the smoothing parameter $h$ . The scores on the ordinate are only defined up to an arbitrary constant equal to the sum of squares of the true (but unknown) PDF [see Fig. 9 and Eqs. (A.1) and (A.2) in Kimoto and Ghil (1993a)]. . . . .	42
4	Estimated PDF of the zonal-flow profile. (a) Two-dimensional PDF on a plane spanned by EOF-1 and EOF-2, with a smoothing parameter $h = 0.4$ ; axes are scaled by the standard deviation of PC-1 and contours are drawn from 0.04 with interval 0.04. The symbol '+' denotes regime centroids (see text for details). (b) Number, out of 100, of random PDFs that fell short of the PDF values shown in (a). Contour interval is 10 and the regions with values larger than 95 are shaded. . . . .	43
5	Same as Fig. 4a but for the quasi-stationary dataset. . . . .	44
6	Cross-validated log-likelihood per sample as a function of the number of clusters, computed by randomly dividing the dataset into two equal partitions 20 times; see Smyth et al. (1999) for details. . . . .	45
7	Mixture model estimates of regime centroids, denoted by the symbol *, and covariance ellipses, superimposed on the data scatter. Only every 50th data point has been plotted for clarity. . . . .	46

8	Composites of zonally and vertically averaged (a) total and (b) anomalous zonal-wind profile that belongs to the regime events. . . . .	47
9	Composites of zonal mean wind at the two model levels for the (a) low- and (b) high-latitude regime events. . . . .	48
10	Duration of recurrent episodes of zonally and vertically averaged zonal flow. . . . .	49
11	Composite anomalies with respect to standardized regime evolution: (a) and (b) vertically averaged zonal mean wind; (c) and (d) vertical wind shear; (e) and (f) vertically averaged eddy momentum flux convergence; and (g) and (h) low-level eddy heat flux. The left panels are for the low-latitude regime and the right panels for the high-latitude regime. Regime onset and break correspond to nondimensionalized time 0 and 10, respectively. The contour interval in (a) and (b) is $1.0 \text{ ms}^{-1}$ , in (c) and (d) is $0.5 \text{ ms}^{-1}$ , in (e) and (f) is $2.5 \times 10^{-6} \text{ ms}^{-2}$ , and in (g) and (h) is $0.5 \text{ Kms}^{-1}$ . Solid contours are positive, dashed ones are negative, and zero contour is omitted. Shaded areas are statistically significant at the 95% level (see text for details). . . . .	50
12	Composites of a root-mean-square (RMS) measure of acceleration of zonal mean wind, with respect to standardized regime evolution. This measure of acceleration is defined by the RMS difference between two meridional profiles, two days apart, of zonally and vertically averaged zonal wind, divided by the time elapsed. Onset and break correspond to the normalized epochs of 0 and 10 days, respectively. Dashed lines indicate a 95% confidence interval for the estimated climatological mean value of the RMS acceleration. . . . .	51
13	Composite anomalies in energetics with respect to standardized regime evolution: (a) zonal-mean available potential energy (APE); (b) total eddy energy, i.e. eddy APE plus eddy kinetic energy (KE); and (c) zonal-mean KE. Onset and break correspond to normalized time 0 and 10, respectively. . . . .	52

14	Dependence of the latitudinal position of the preferred regimes' zonal-jet maximum on bottom friction. . . . .	53
----	---	----

Table 1: Probability of regime transitions.

	All the regime <i>episodes</i>			Regime <i>events</i> only		
From/To	1	2	3	1	2	3
1	0.28	0.32	0.40	0.22	0.41	0.37
2	0.22	0.68	0.10	0.04	0.67	0.29
3	0.12	0.16	0.72	0.03	0.28	0.69

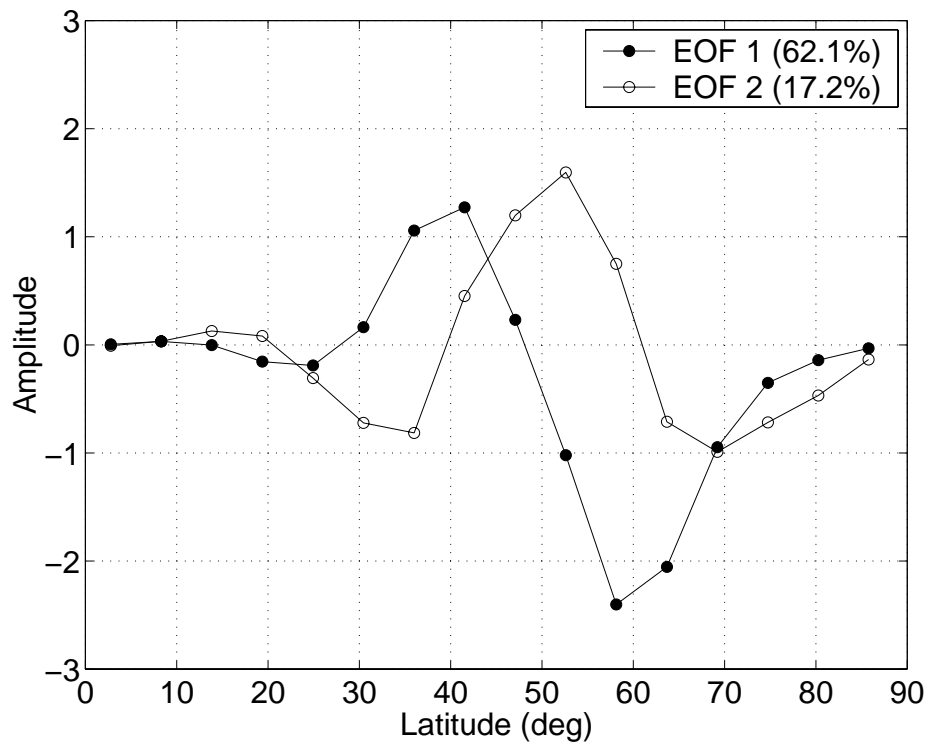


Figure 1: The two leading EOFs of the 10-day low-pass filtered zonally and vertically averaged zonal flow.



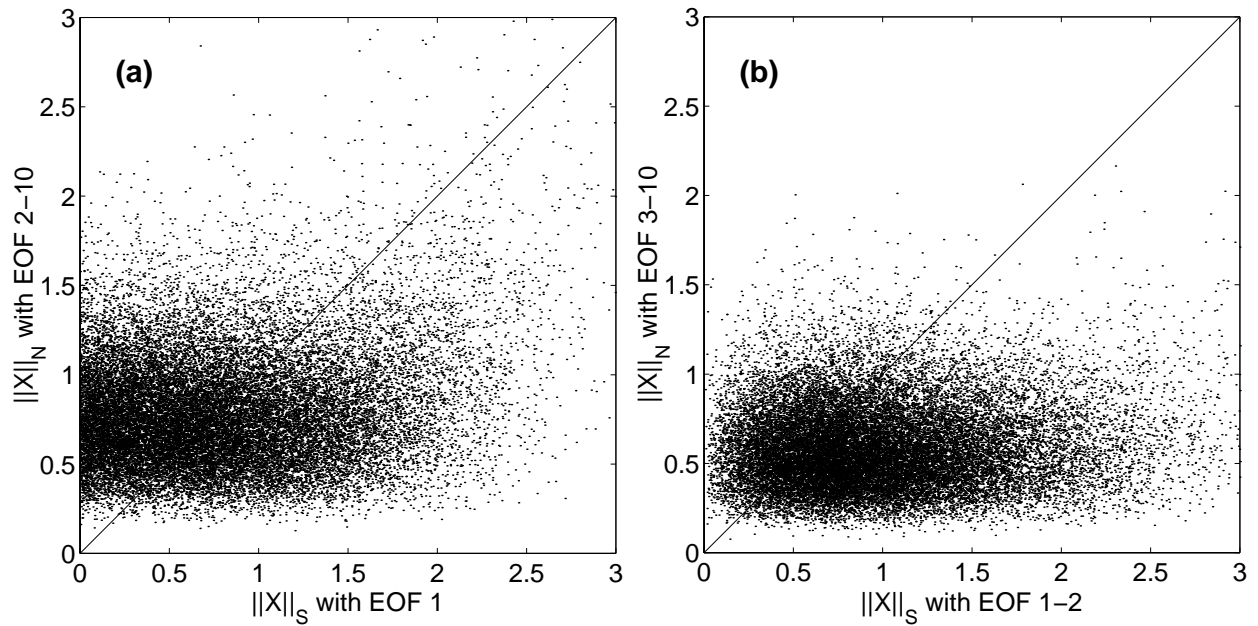


Figure 2: Data scatter in terms of leading EOFs. (a) Abscissa is the root-mean square (RMS) magnitude of anomalies in phase space computed with only PC-1, and ordinate is the RMS magnitude of anomalies with PC-2 through PC-10. (b) Abscissa is the RMS magnitude of anomalies computed with PC-1 and PC-2, and ordinate is the RMS magnitude of anomalies with PC-3 through PC-10.

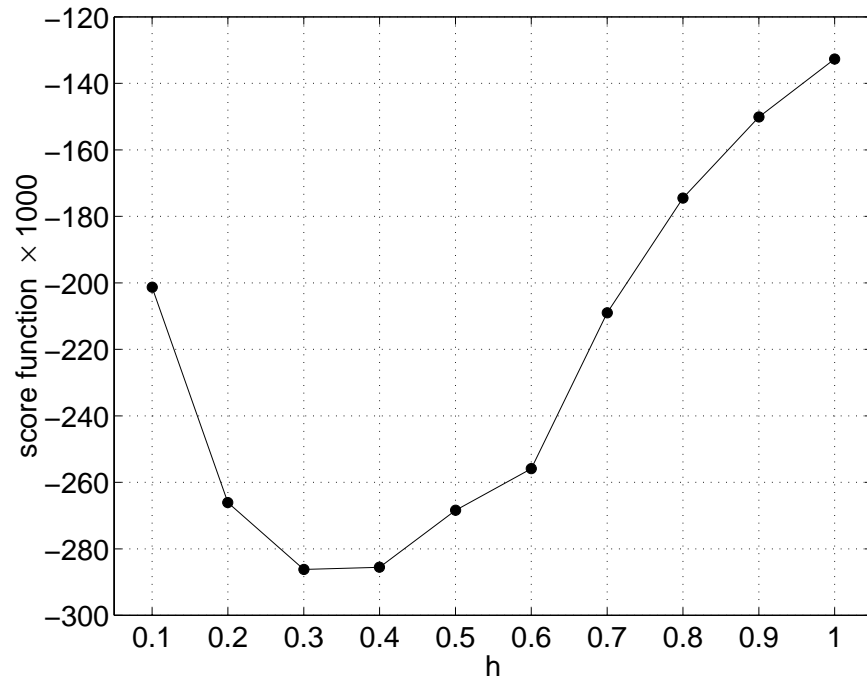


Figure 3: Least-squares cross validation (LSCV) scores as a function of the smoothing parameter  $h$ . The scores on the ordinate are only defined up to an arbitrary constant equal to the sum of squares of the true (but unknown) PDF [see Fig. 9 and Eqs. (A.1) and (A.2) in Kimoto and Ghil (1993a)].

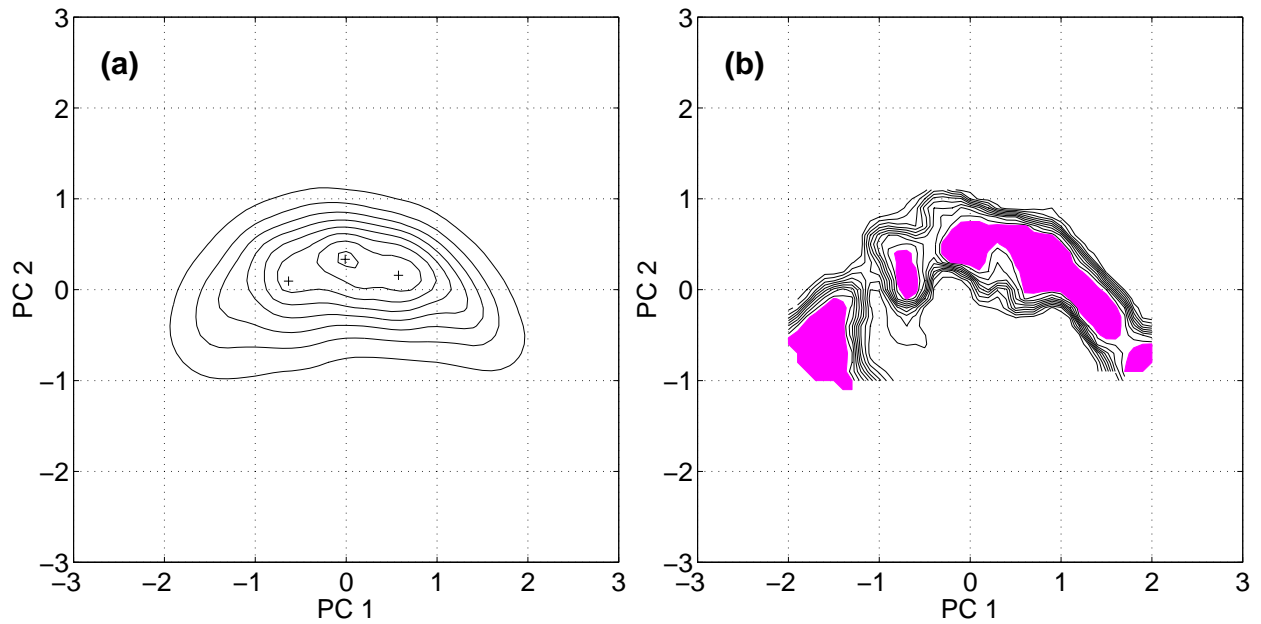


Figure 4: Estimated PDF of the zonal-flow profile. (a) Two-dimensional PDF on a plane spanned by EOF-1 and EOF-2, with a smoothing parameter  $h = 0.4$ ; axes are scaled by the standard deviation of PC-1 and contours are drawn from 0.04 with interval 0.04. The symbol '+' denotes regime centroids (see text for details). (b) Number, out of 100, of random PDFs that fell short of the PDF values shown in (a). Contour interval is 10 and the regions with values larger than 95 are shaded.

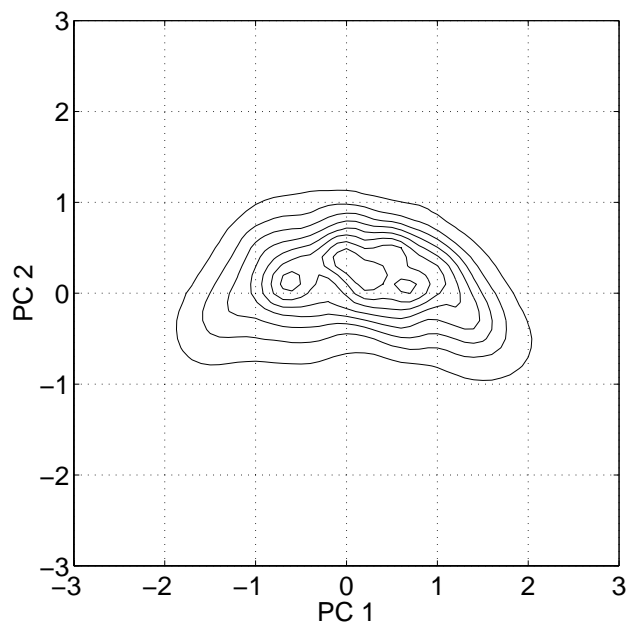


Figure 5: Same as Fig. 4a but for the quasi-stationary dataset.

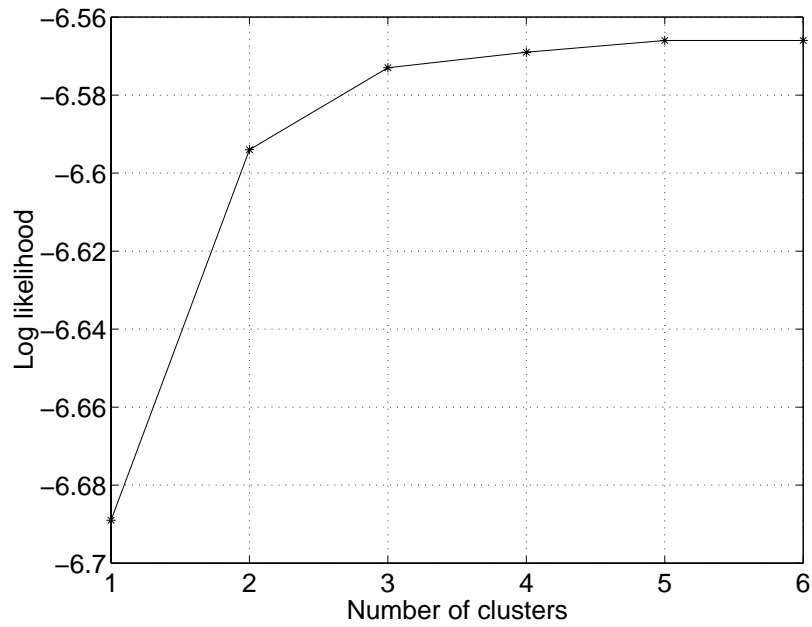


Figure 6: Cross-validated log-likelihood per sample as a function of the number of clusters, computed by randomly dividing the dataset into two equal partitions 20 times; see Smyth et al. (1999) for details.

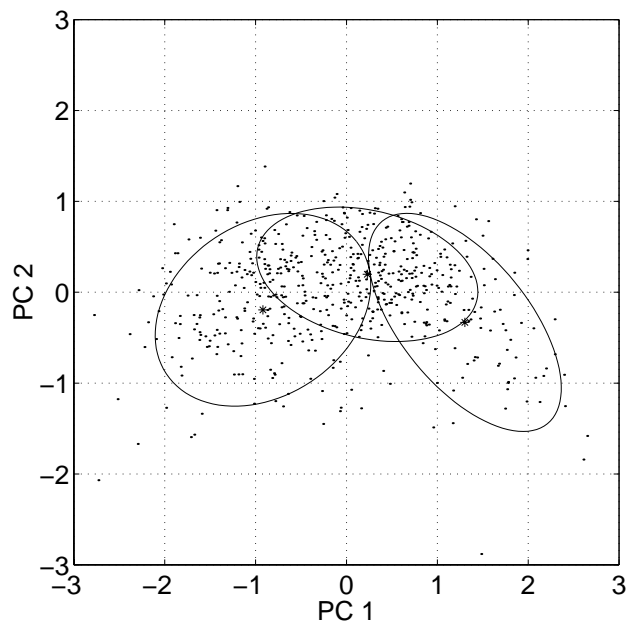


Figure 7: Mixture model estimates of regime centroids, denoted by the symbol \*, and covariance ellipses, superimposed on the data scatter. Only every 50th data point has been plotted for clarity.

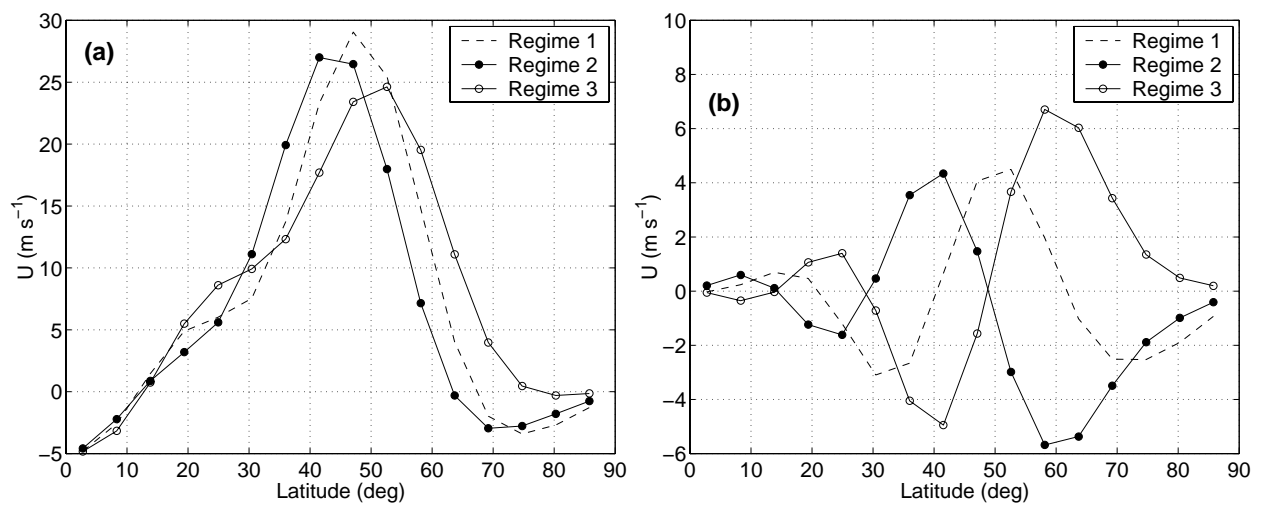


Figure 8: Composites of zonally and vertically averaged (a) total and (b) anomalous zonal-wind profile that belongs to the regime events.

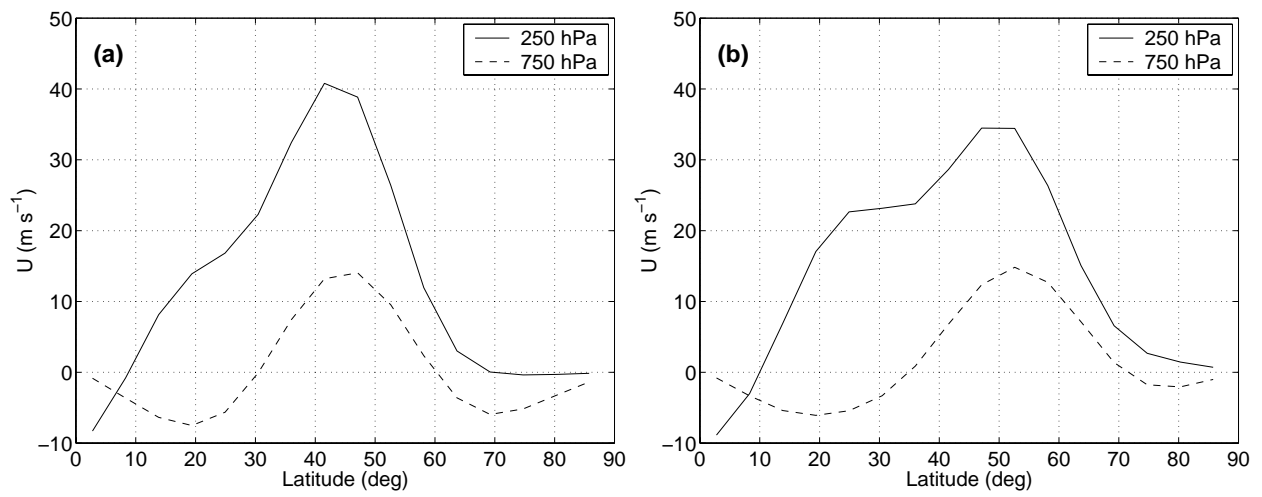


Figure 9: Composites of zonal mean wind at the two model levels for the (a) low- and (b) high-latitude regime events.



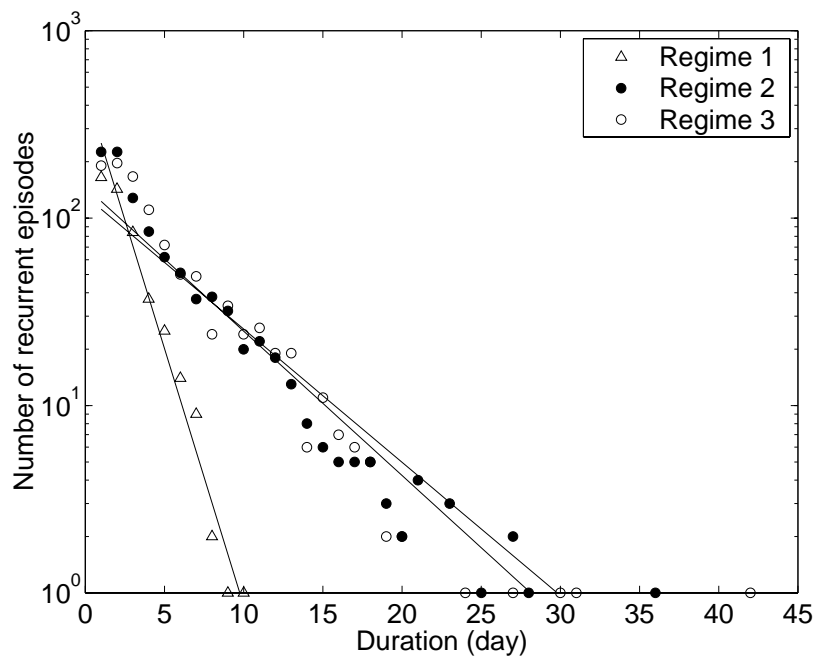


Figure 10: Duration of recurrent episodes of zonally and vertically averaged zonal flow.

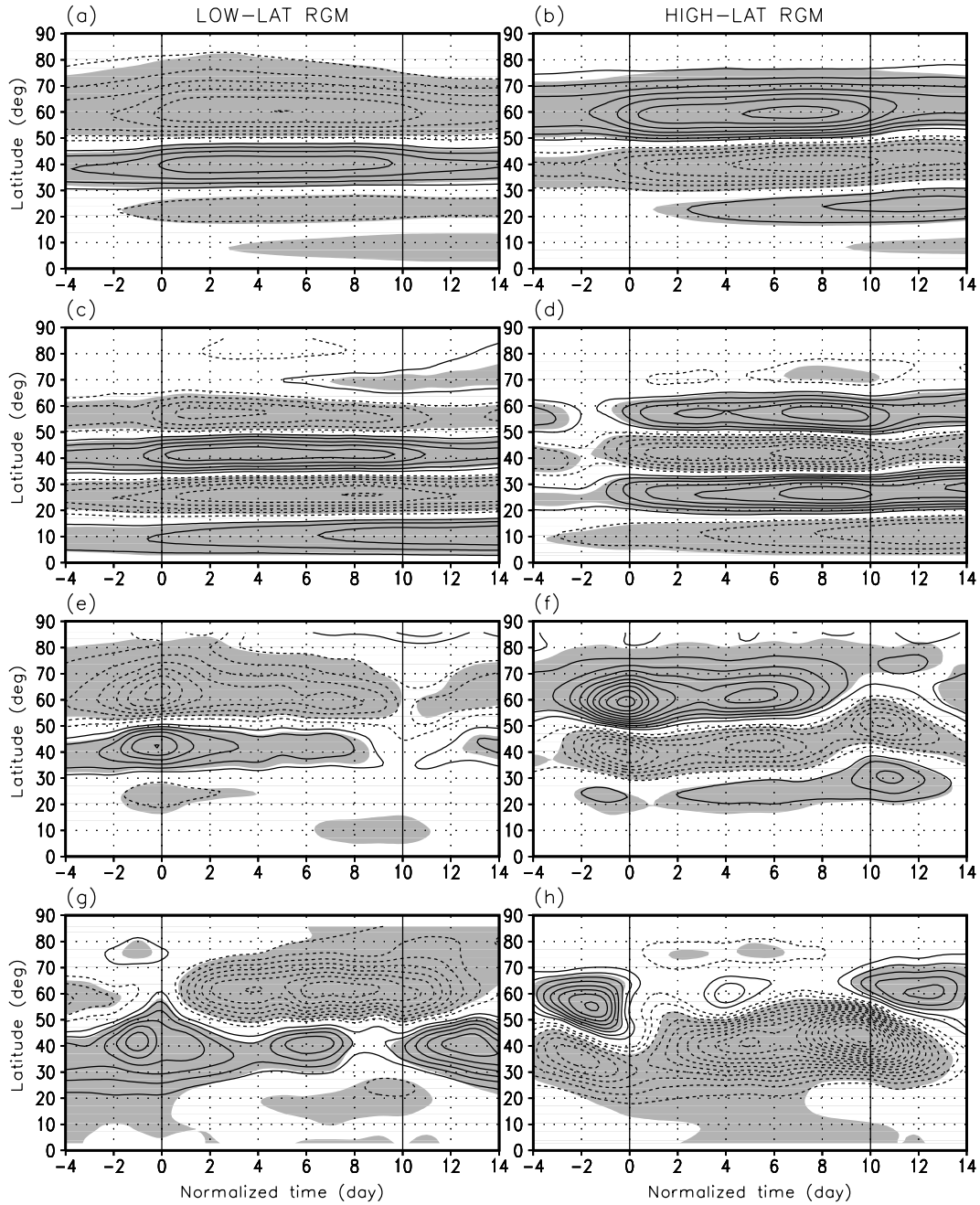


Figure 11: Composite anomalies with respect to standardized regime evolution: (a) and (b) vertically averaged zonal mean wind; (c) and (d) vertical wind shear; (e) and (f) vertically averaged eddy momentum flux convergence; and (g) and (h) low-level eddy heat flux. The left panels are for the low-latitude regime and the right panels for the high-latitude regime. Regime onset and break correspond to nondimensionalized time 0 and 10, respectively. The contour interval in (a) and (b) is  $1.0 \text{ ms}^{-1}$ , in (c) and (d) is  $0.5 \text{ ms}^{-1}$ , in (e) and (f) is  $2.5 \times 10^{-6} \text{ ms}^{-2}$ , and in (g) and (h) is  $0.5 \text{ Kms}^{-1}$ . Solid contours are positive, dashed ones are negative, and zero contour is omitted. Shaded areas are statistically significant at the 95% level (see text for details).

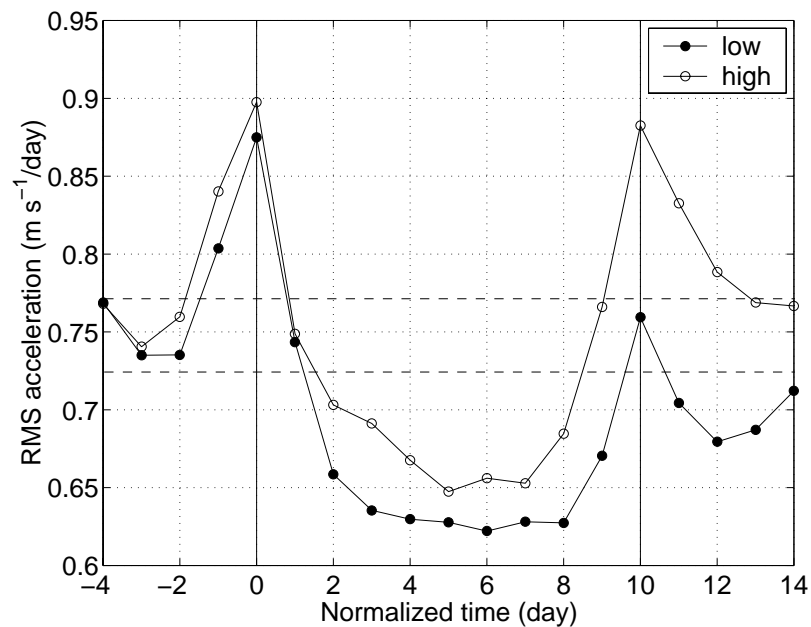


Figure 12: Composites of a root-mean-square (RMS) measure of acceleration of zonal mean wind, with respect to standardized regime evolution. This measure of acceleration is defined by the RMS difference between two meridional profiles, two days apart, of zonally and vertically averaged zonal wind, divided by the time elapsed. Onset and break correspond to the normalized epochs of 0 and 10 days, respectively. Dashed lines indicate a 95% confidence interval for the estimated climatological mean value of the RMS acceleration.

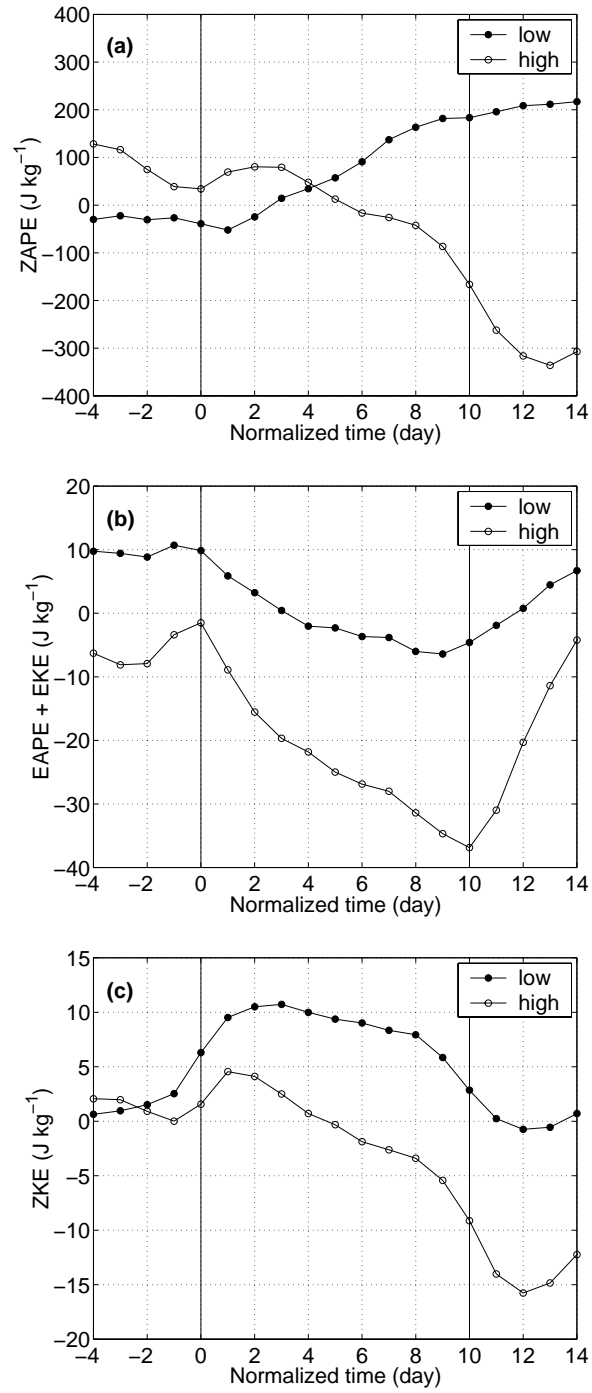


Figure 13: Composite anomalies in energetics with respect to standardized regime evolution: (a) zonal-mean available potential energy (APE); (b) total eddy energy, i.e. eddy APE plus eddy kinetic energy (KE); and (c) zonal-mean KE. Onset and break correspond to normalized time 0 and 10, respectively.

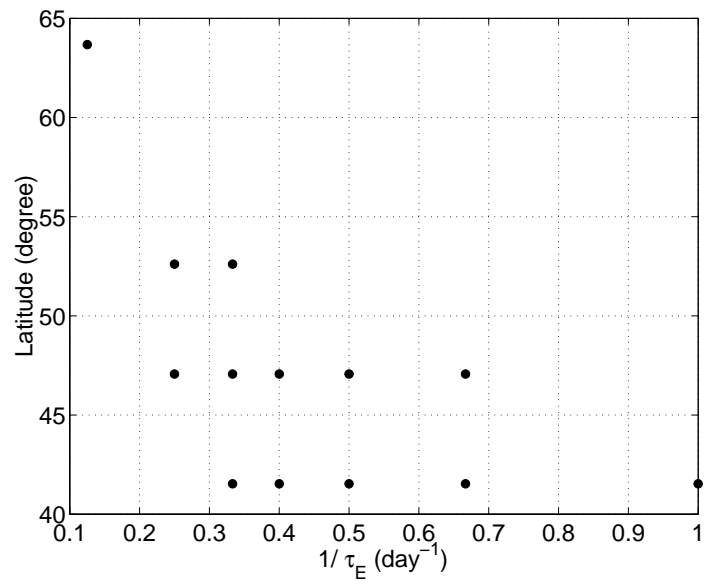


Figure 14: Dependence of the latitudinal position of the preferred regimes' zonal-jet maximum on bottom friction.